

Platinum/Apatite Water-Gas Shift Catalysts

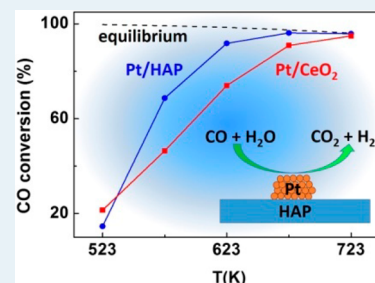
Dengyun Miao, Andreas Goldbach,* and Hengyong Xu

Dalian National Laboratory for Clean Energy, Dalian Institute of Chemical Physics, Chinese Academy of Sciences, 457 Zhongshan Road, 116023 Dalian, People's Republic of China

Supporting Information

ABSTRACT: Water-gas shift (WGS) micro and membrane reactors are interesting components for compact H₂ production and purification devices, but they require catalysts with very high activity for optimum efficiency to minimize catalyst bed thickness and mass transfer limitations. On the other hand, activation of H₂O is known to be more challenging than CO in this reaction. Catalysts comprising ca. 2 nm large Pt particles on hydrophilic apatites are found to have very high WGS activity, with specific reaction rates exceeding those of a highly active Pt/CeO₂ catalyst by up to 50% at 573 K. These apatite-supported catalysts exhibit stable CO conversions at 673 K without showing any CH₄ formation tendencies up to 723 K. WGS activity increases with Ca/P ratio in the apatite, leveling off around Ca/P ≈ 1.75, and formate has been identified as the main reaction intermediate. The outstanding WGS performance is attributed to the superior activation of H₂O on these ionic oxides due to coordination of H₂O to Lewis acidic Ca²⁺ ions and H bonding to basic O atoms of PO₄³⁻ units. This renders H₂O molecules highly polarized and thus reactive on apatite surfaces with the ensuing formate-like intermediates being well stabilized through bonding to multiple Ca²⁺ ions, as well. Thus, apatites provide an intriguing alternative to increasingly expensive rare-earth oxides in high-performance noble-metal WGS catalysts not only for micro and membrane reactors.

KEYWORDS: high-temperature water-gas shift, H₂O activation, formate intermediates, ionic oxides, reaction rate, activation energy



INTRODUCTION

The water-gas shift (WGS) reaction ($\text{CO} + \text{H}_2\text{O} \rightleftharpoons \text{CO}_2 + \text{H}_2$, $\Delta H = -41.1 \text{ kJ mol}^{-1}$) is an important industrial process which has attracted renewed attention in recent years in connection with on the spot hydrogen production for fuel cells in transportation and residential applications. Industrially it is carried out in two stages: i.e., a high-temperature shift (HTS) over Fe–Cr catalysts at 593–723 K followed by a low-temperature shift (LTS) over Cu–Zn–Al catalysts at 473–523 K.¹ However, these conventional catalysts are unsuitable for compact hydrogen generation systems as desired for fuel cell applications because of their weight and volume, long start-up times, durability under steady-state and transient conditions, and susceptibility to condensation and poisoning.^{2,3} Therefore, precious metals supported on ceria and other reducible oxides have been widely investigated, in particular as LTS catalysts for fuel cell applications.^{2–7} Highly active WGS catalysts are also required for achieving optimum efficiency with HTS micro-reactors⁸ and Pd membrane reactors.⁹ For example, computational simulations show that an optimum membrane would improve the efficiency of WGS Pd membrane reactors only by 12%, whereas 76% could be gained by optimizing the catalyst.¹⁰ Operation temperatures above 623 K are especially favorable in the latter case, because hydrogen-selective Pd membranes are significantly inhibited by CO below that threshold.¹¹ However, many precious-metal catalysts on reducible supports are not sufficiently stable and progressively deactivate under typical reformer outlet conditions.¹² On the other hand, cost is a major concern, since noble metals and rare-earth elements are

expensive, so that current research aims at reducing the amounts of both in catalyst formulations.¹³

We are now investigating the HTS activity and stability of Pt supported on hydroxyapatite ($\text{Ca}_{10}(\text{PO}_4)_6(\text{OH})_2$, HAP) because Au and Ru deposited on this irreducible ionic oxide showed LTS activity before.¹⁴ The Au catalyst had been more active than the Ru catalyst up to 593 K, but high-temperature WGS activity and stability of the Au catalyst was not reported while the Ru catalyst showed serious methanation activity above 573 K.¹⁴ Apatites and related compounds are intriguing support materials for catalysts because of their structural stability, their hydrophilicity due to amphoteric acid and base functionalities, and the possibility of cationic and anionic isomorphous substitutions.^{15–27} For example, hydroxide and phosphate ions were found to stabilize Au nanoparticles against sintering at elevated temperatures.¹⁵ We focused on Pt catalysts in our study because of their generally superior high-temperature stability in comparison to e.g. Au WGS catalysts.²⁸ The catalytic activity of apatite catalysts can be substantially modulated by changing the Ca/P ratio.^{16–19} This results in nonstoichiometric formulations $\text{Ca}_{10-Z}(\text{HPO}_4)_Z(\text{PO}_4)_{6-Z}(\text{OH})_{2-Z}$ with $0 \leq Z \leq 1$, i.e. $1.50 \leq \text{Ca/P} \leq 1.67$. Hydroxyapatites with larger than stoichiometric Ca/P ratio (1.67) have been also reported where excess Ca²⁺ ions may be charge balanced by carbonate or other foreign anions.²⁰

Received: August 28, 2015

Revised: December 20, 2015

Therefore, we have explored the interdependence between apatite stoichiometry and WGS activity of such Pt catalysts by preparing HAP formulations with Ca/P ratios ranging between 1.58 and 2.00, and a fluoroapatite (FAP) form where hydroxide ions were replaced by fluoride ions. In the following we will show that catalysts can be designed in this way that feature HTS activities exceeding those of Pt on CeO₂ and other reducible oxides and at the same time exhibit very good HTS stability.

■ EXPERIMENTAL SECTION

Catalyst Preparation. All chemicals were of analytical grade, were used without further purification, and were procured from Kermel unless otherwise noted. Hydroxyapatite powders were synthesized by a precipitation method^{15,23} using aqueous solutions of Ca(NO₃)₂·4H₂O and (NH₄)₂HPO₄ as precursors and aqueous ammonia (25%) for adjustment of the pH value of the solutions between 9 and 10.5. Typically 100 mL of a 0.20 mol L⁻¹ (NH₄)₂HPO₄ aqueous solution (e.g., at pH 9) was added dropwise to 100 mL of 0.33 mol L⁻¹ Ca(NO₃)₂ aqueous solution (e.g., at pH 9) with vigorous magnetic stirring at room temperature. The resulting suspension was kept in a water bath for 2 h at 363 K and then cooled to room temperature and aged for 6 h. Next the precipitate was centrifuged, washed repeatedly with purified water until pH ~7, dried at 333 K for 12 h, and finally calcined for 4 h in air at 753 K in a muffle furnace. The obtained HAP powders were denoted HAP-9, HAP-9.5, HAP-10, and HAP-10.5 according to the pH of the synthesis solutions. Further HAP-9 and HAP-10 powders with modified Ca content were made by wet impregnation of the calcined materials with Ca(NO₃)₂ solution. Those samples were denoted Ca-HAP-9 and Ca-HAP-10, respectively. Fluoride-substituted apatite (denoted as FAP) was prepared by adding 0.247 g of NH₄F to the (NH₄)₂HPO₄ solution before combination with the Ca(NO₃)₂ solution (both at pH 10). The remaining procedural steps were the same as for preparation of the HAP powders.

Catalysts with nominally 1 wt % Pt were prepared by impregnation of the calcined apatite powders. Appropriate amounts of 15.8 mg mL⁻¹ aqueous H₂PtCl₆ (Sinopharm Chemical Reagent Co.) were added, and suspensions were kept at room temperature for about 24 h before samples were dried at 333 K for 12 h and calcined again for 4 h in air at 753 K in a muffle furnace. For comparison, 1 wt % Pt/CaO, Pt/CaCO₃, Pt/γ-Al₂O₃ and Pt/CeO₂ catalysts were prepared by incipient wetness impregnation with aqueous H₂PtCl₆ in addition. Preparation of the Pt/CeO₂ catalyst has been described elsewhere in detail.²⁹ CeO₂ was obtained by calcination of Ce(NO₃)₃·6H₂O (Sinopharm) at 723 K for 4 h in a muffle furnace. γ-Al₂O₃ was prepared by calcination of pseudo boehmite (Shandong Aluminum Co.) at 773 K for 4 h in a muffle furnace.

Catalyst Characterization. X-ray diffraction (XRD) patterns of the catalyst powders were recorded on a PANalytic X'Pert Pro-I instrument using Cu Kα radiation (λ = 0.1541 nm). The bulk Ca/P ratio and Pt content were analyzed with an inductively coupled plasma optical emission spectrometer (ICP-OES, PerkinElmer Optima 7300DV) after the catalyst samples had been digested with aqua regia at room temperature. The specific surface area was analyzed by N₂ adsorption at 77 K using a QuadraSorb SI instrument (Quantachrome). All samples were used as powders and degassed at 573 K for 6 h under vacuum before N₂ adsorption and pore sizes were

determined from the desorption branch of the isotherms. Platinum dispersions were derived from H₂ and CO chemisorption measurements at 323 K using an AutoChem 2910 system (Micromeritics) assuming that the molar ratio of adsorbed H₂ to exposed Pt is 0.5 and 1 for adsorbed CO to exposed Pt. Each catalyst (50 mg) was first reduced in 10% H₂/Ar at 573 K for 1 h, heated to 698 K under Ar (He) and kept at that temperature for 1 h, and then cooled to 323 K in Ar (He). Chemisorption measurements were performed at that temperature by injecting a series of 10% H₂/Ar (5% CO/He) pulses until saturation adsorption was reached. Transmission electron microscopy (TEM) images were obtained on a JEM-2100 system (JEOL) with an acceleration voltage of 200 kV. The samples were ultrasonically suspended in ethanol and placed onto a carbon film supported over a Cu grid for that purpose.

Fourier transform infrared (FTIR) spectra were recorded in the 400–4000 cm⁻¹ range at a resolution of 4 cm⁻¹ on a Bruker Tensor 27 spectrometer equipped with a deuterated triglycine sulfate (DTGS) detector. Carefully ground catalyst samples were diluted with KBr (mass ratio 1:100) and pressed into self-supporting wafers (13 mm diameter) for ex situ measurements in air. Undiluted catalysts were pressed into self-supporting wafers, and the DTGS detector was replaced by a mercury–cadmium–telluride (MCT) detector for in situ FTIR spectroscopic analyses under WGS conditions using a quartz cell equipped with CaF₂ windows. Wafers were reduced in H₂ at 573 K for 0.5 h and then purged in N₂ at 723 K for 0.5 h and finally cooled to 523 K in N₂ before in situ measurements with a 1.9% CO/3.2% H₂O/He mixture that had been produced by bubbling a 2% CO/He mixture through water at room temperature.

X-ray photoelectron spectroscopy (XPS) experiments were carried out on a Thermo ESCALAB 250Xi instrument to determine the molar ratios of elements at the catalyst surface using Al Kα radiation (hν = 1486.6 eV). The C 1s peak was set at 284.8 eV and taken as reference for binding energy calibration. Temperature-programmed reduction (TPR) was carried out in a homemade system furnished with a thermal conductivity (TCD) detector. All TPR samples were pretreated in Ar at 473 K for 2 h, cooled to room temperature, and then heated in 5% H₂/Ar at a rate of 10 K min⁻¹. The TCD detector was calibrated by reducing 5 mg of CuO to Cu for quantification of H₂ consumption during TPR. Carbon deposition after catalytic testing was probed by temperature-programmed oxidation (TPO) in a home-built setup equipped with a Pfeiffer OmniStar mass spectrometer (MS) to detect CO (28), CO₂ (44), O₂ (32), and H₂O (18). Values in parentheses are monitored mass/charge ratios (*m/z*).

Catalytic Testing. WGS activity tests were carried out in a fixed-bed quartz reactor with a diameter of 8 mm at atmospheric pressure and temperatures between 523 and 723 K. The calcined catalysts were ground to powder, pressed into a pellet at 20 MPa, crushed, and sieved. The particle size used for catalytic testing was 40–60 mesh (250–380 μm particles). Typically 75 mg of catalyst was diluted with 100 mg of quartz sand of the same particle size range and loaded into the quartz reactor. The height of the catalyst bed was about 5 mm. The reactor was heated under He to 523 K before the reactants were introduced. Water was injected into a preheater with a calibrated double-plunger pump (Elite P230), where it was vaporized and mixed with the dry feed gas components. The gas mixture for product-free activity tests consisted of 5% CO, 20% H₂O, and 75% He. Those measurements were carried out

Table 1. Characteristic Properties of Catalysts

sample	pH ^a	S _{BET} ^b (m ² g ⁻¹)	Pt ^c (wt %)	dispersion ^d (%)	d _{Pt} ^d (nm)	Ca/P molar ratio	
						ICP	XPS
Pt/HAP-10.5	10.5	71	0.77	100	1.1	1.76	
				86 ^e	1.3 ^e		
Pt/HAP-10	10	71	0.74	96	1.2	1.75	1.64
Pt/HAP-9.5	9.5	85	0.78	73	1.6	1.68	1.51
Pt/HAP-9	9	77	0.82	81	1.4	1.58	1.45
Pt/FAP	10	73	0.78	101	1.1	1.75	
Pt/CeO ₂		83	0.74	150	0.8		
				58 ^e	1.9 ^e		
Pt/Ca-HAP-9	9		0.73			1.74	
Pt/Ca-HAP-10	10		0.79			2.00	

^aApatite synthesis pH. ^bSupport surface area (without Pt). ^cICP-OES analysis. ^dH₂ chemisorption. ^eCO chemisorption.

at GHSV = 150000 mL g_{cat}⁻¹ h⁻¹. A reformat type gas mixture (15% CO, 5% CO₂, 30% H₂O, 40% H₂, 10% N₂) was used for determination of specific reaction rates *r* and a long-term stability test. The reactor tail gas was passed through a cooling trap, where excess steam was condensed. The dry tail gas was then fed to a gas chromatograph (Shimadzu GC-8A) equipped with a TCD for CO, CO₂, and CH₄ analysis.

The 100–160 mesh fraction (96–150 μm particle size) of the catalysts was diluted with quartz sand particles in the same size range (100–160 mesh) and used for measurement of specific reaction rates. The amount of catalyst was varied (20–200 mg) to limit CO conversion to 20% at maximum. The height of the catalyst bed was about 8 mm. Samples were subjected to 12 h of conditioning in the product-free feed mixture at 673 K before these measurements. At each reaction temperature the tail gas was analyzed at different reaction times to calculate CO conversion. No methane was observed during measurement of the specific rates. Conversion of CO (*X*_{CO}) was calculated according to

$$X_{\text{CO}} = \frac{[\text{CO}]_{\text{in}} - [\text{CO}]_{\text{out}}}{[\text{CO}]_{\text{in}}} \quad (1)$$

where [CO]_{in} and [CO]_{out} are CO concentrations in feed and tail gas, respectively. Thermodynamic equilibrium WGS CO conversions *X*_{CO,eq} were calculated in an analogous manner by replacing [CO]_{out} in eq 1 with WGS equilibrium concentrations [CO]_{eq} that were computed with the program Gaseq (<http://www.arcl02.dsl.pipex.com/>).

RESULTS

Catalyst Characteristics. Table 1 summarizes physico-chemical properties of the prepared apatite and Pt/apatite materials. All diffraction patterns (Figure S1 in the Supporting Information) correspond with the apatite structure (JCPDS 01-074-0566).^{18,19} No diffraction peaks resulting from Pt or its oxides were observed for any Pt/apatite sample, indicating that the particle size of Pt species remained below the XRD detection limit (ca. 4 nm). Apatite crystallinity improved with increasing pH of the synthesis solution according to the width and resolution of the Bragg reflections. Note that mixed-phase structures including HAP precipitated at pH ≤ 8.5. Lattice parameters *a* and *c* of the Pt/HAP-*X* and Pt/FAP samples matched very well with those of standard apatite patterns (Table S1 in the Supporting Information). Chemical analyses confirmed that the Ca/P molar ratio of the apatite materials (Table 1) increased with increasing synthesis pH value, as

reported in the literature.¹⁸ Hydroxyapatite with stoichiometric composition (Ca/P = 1.67) formed at pH 9.5. The Ca/P ratio did not exceed 1.75 in the precipitated apatite materials, but it was increased up to 2.00 via subsequent impregnation of as-synthesized materials with Ca(NO₃)₂ solutions. The surface Ca/P ratios resulting from XPS analyses (Table 1) were smaller than the bulk values, in agreement with previous studies.^{18,19,26}

Textural properties of the apatite materials were determined prior to impregnation with Pt. All adsorption–desorption isotherms belong to type IV (Figure S2a in the Supporting Information). The specific surface area *S*_{BET} ranged between 71 and 85 m² g⁻¹ (Table 1). Similar *S*_{BET} values have been reported in the literature.^{15,22} Substitution of hydroxide with fluoride ions did not have an obvious impact on the surface area. Interparticle pore size distributions (Figure S2b) were in the typical range reported for apatite-supported catalysts^{19–25} although noticeably reduced in FAP (5–20 nm) in comparison to the HAP materials (10–30 nm). The noble-metal content of all Pt/apatite catalysts was somewhat less than the targeted amount, albeit very similar (0.73–0.82%, Table 1) according to ICP-OES analyses. TEM showed that Pt was well dispersed on the apatite catalysts (Figure S3 in the Supporting Information) with most noble-metal clusters being smaller than 2 nm, in good agreement with mean particle diameters and dispersions derived from H₂ and CO chemisorption (Table 1).

Unfortunately, analysis of Pt particle size was not as straightforward for the Pt/CeO₂ catalyst, although from the absence of Pt XRD peaks it is clear that Pt aggregates were smaller than ~4 nm there as well. Platinum particles could not be detected by TEM due to a lack of contrast³⁰ between them and the CeO₂ support. Hydrogen chemisorption is also not well suited for determining metal dispersions on reducible oxides such as CeO₂ because concomitant surface reduction of the latter insinuates often exceedingly high dispersion values as for the present Pt/CeO₂ catalyst (Table 1).³⁰ Carbon monoxide chemisorption yielded 58% Pt dispersion, but that method is not very accurate either when dealing with reducible oxides: Reactive CO adsorption at surface hydroxyl groups can lead to overestimation³¹ of metal dispersion, while strong metal support interaction in such materials can result in much too large Pt particle size estimates³² as we previously experienced.³³ Thus, we consider the 1.9 nm resulting from CO chemisorption as an upper limit for Pt particle size with the lower limit of 1.1 nm following from 100% Pt dispersion. Accordingly, the mean Pt particle size was not very different if at all on Pt/CeO₂ from that on the apatite-supported catalysts. Figure 1 and Figure S4 in the Supporting Information show FTIR spectra of the Pt/

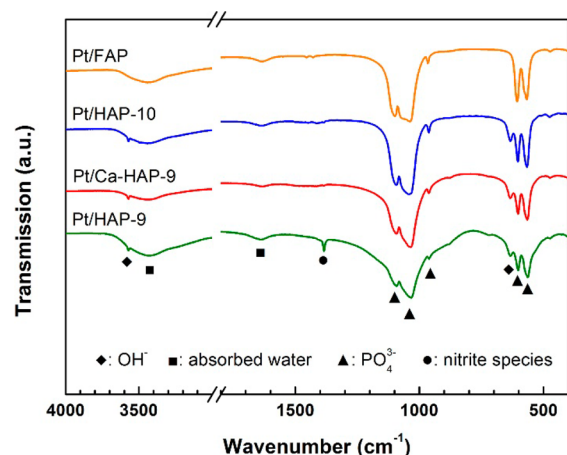


Figure 1. Infrared spectra of Pt/HAP-10, Pt/HAP-9, Pt/Ca-HAP-9, and Pt/FAP catalysts.

HAP-X and Pt/FAP materials which are rather similar and are in good agreement with reported apatite IR spectra. The bands at 576, 603, 962, 1041, and 1095 cm^{-1} are due to bending and stretching vibrational modes of the PO_4^{3-} tetrahedra.^{20,34} These bands are considerably broadened in the samples prepared at pH 9 and 9.5 (Figure S4), which hints at structural disorder and is likely related to the lower crystallinity of these materials (Figure S1 in the Supporting Information). Interestingly, the broadening of the PO_4^{3-} bands disappeared after impregnation of Pt/HAP-9 with additional Ca^{2+} ions. In fact, the FTIR spectrum of Ca-impregnated Pt/Ca-HAP-9 was practically identical with that of Pt/HAP-10 (Figure 1). Weak bands at 1450 and 1413 cm^{-1} can be attributed to carbonate species^{20,35} which might have originated from CO_2 adsorption during preparation or subsequent handling in air. The band at 1385 cm^{-1} can be assigned to nitrite species³⁶ resulting from incomplete decomposition of residual nitrate from the synthesis solution during calcination. Broad bands at 3446 and 1637 cm^{-1} are due to adsorbed water.³⁷ The characteristic OH^- librational and stretching bands^{20,38} at 632 and 3572 cm^{-1} are missing in the Pt/FAP spectrum. This indicates that OH^- ions inside the channels of the HAP structure can be completely substituted by F^- ions, in agreement with literature reports.^{34,39,40}

Figure 2 shows H_2 TPR spectra of Pt/HAP-10 and Pt/FAP and the corresponding noble-metal-free materials. There was no appreciable H_2 consumption up to 973 K in case of the fluoroapatite and also HAP-9 and HAP-9.5 (Figure S5 in the Supporting Information), while the other apatite materials yielded weak reduction peaks around 723 K (773 K for HAP-10.5; Figure S5) and stronger peaks around 923 K. In general, Pt reduction started around 323 K, yielding a first maximum or shoulder around 358–366 K and then two strong H_2 consumption peaks around 483 K and 673–713 K, although the weak initial maximum was missing and the second strong reduction feature shifted to lower temperatures (608–678 K) in the case of HAP-9 and HAP-9.5. These patterns are similar to those reported by Takarroumt et al. for a series of Pt/HAP catalysts with $\text{Ca/P} \approx 1.60$ and 0.42–2.40% Pt, although the second strong Pt reduction peak above 573 K was observed only at higher Pt loadings.²⁴ They attributed H_2 consumption below that temperature to reduction of Pt oxides and Pt^{2+} ions on the surface and within the apatite lattice and H_2 uptake at higher temperatures to adsorption of hydrogen on the reduced

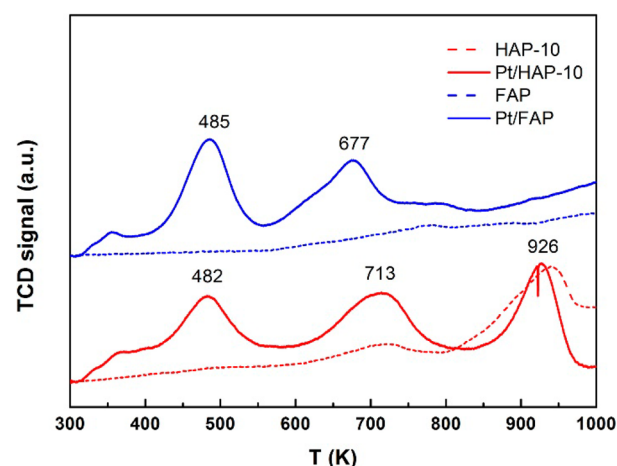


Figure 2. Temperature-programmed reduction spectra of HAP, FAP, and corresponding Pt catalysts.

Pt. However, quantitative analysis of H_2 uptake (Table S2 in the Supporting Information) would suggest rather high H_2 adsorption on the reduced Pt of the catalysts investigated here ($\text{H}_2/\text{Pt} \approx 1$). On the other hand, similar TPR patterns with two strong H_2 consumption features have been frequently observed for Pt supported on other irreducible support materials and were typically attributed to Pt oxides that interact weakly (ca. 523 K) and strongly (ca. 713–753 K) with the support.^{41–43} Therefore, we attribute the two strong H_2 consumption peaks of our Pt/apatite materials also to reduction of PtO_x species interacting weakly and strongly with the support. Reduction of Pt oxides supported on the apatite materials is apparently somewhat facilitated with respect to e.g. $\gamma\text{-Al}_2\text{O}_3$ ⁴¹ and HZSM-5.^{42,43} Furthermore, the low-temperature H_2 consumption with a maximum below 373 K is most certainly due to Pt^{4+} species, as TPR of PtO_2 yields a reduction peak centered at 368–378 K.⁴⁴ The quantitative H_2 consumption analysis also suggests the presence of highly oxidized Pt species, as total H_2/Pt ratios ranged between 1.5 and 2 for most catalysts (Table S2).

Catalytic Reaction. Figure 3 shows CO conversion over Pt/HAP-X catalysts as a function of temperature in the product-free reaction mixture. Carbon dioxide was the only carbonaceous product over these catalysts: i.e., no CH_4 formation was observed. Catalyst activity increased with Ca/P ratio, with X_{CO} reaching equilibrium conversion over Pt/HAP-

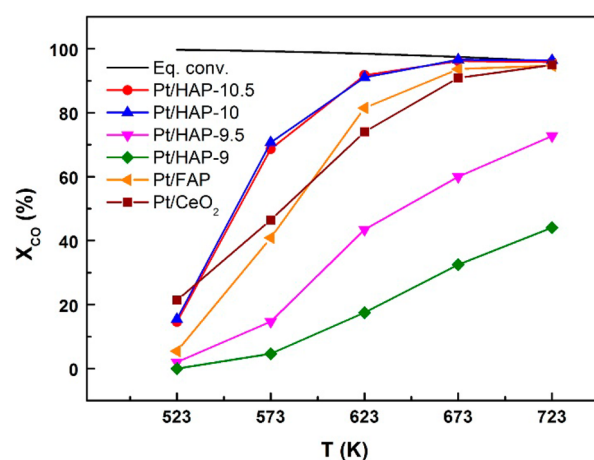


Figure 3. CO conversion over Pt/apatite and Pt/ CeO_2 catalysts.

10 and Pt/HAP-10.5 at 673 K. Moreover, CO conversion over these two catalysts exceeded significantly that over a highly WGS-active Pt/CeO₂ catalyst except at the lowest test temperature. This previously reported Pt/CeO₂ catalyst had the same nominal noble-metal loading.²⁹ In contrast, Pt/HAP-9 and Pt/HAP-9.5 were much less WGS active and X_{CO} did not reach equilibrium even at 723 K. Interestingly, after the Ca/P ratio of Pt/HAP-9 was raised to the same level as that of Pt/HAP-10 via impregnation with Ca(NO₃)₂ solution, CO conversion over Pt/Ca-HAP-9 approached that over Pt/HAP-10 over the entire temperature range (Figure S6 in the Supporting Information). This corroborates that the Ca/P ratio is important for WGS activity of Pt supported on hydroxyapatites even though addition of further Ca to HAP-10 did not trigger a further substantial X_{CO} enhancement (Figure S6, Pt/Ca-HAP-10). Figure 3 shows in addition that CO conversion over Pt/FAP was similar to that over the Pt/CeO₂ reference catalyst. Note that HAP-10 did not exhibit any WGS activity in the range from 523 to 723 K under these test conditions. Furthermore, Pt supported on CaO and CaCO₃ yielded rather low CO conversion in this temperature range (Figure S7 in the Supporting Information). Finally, we tested the WGS activity of nominally 1% Pt on another irreducible support, i.e. γ -Al₂O₃, which also yielded much smaller X_{CO} values than all of the Pt/apatite catalysts except Pt/HAP-9 and Pt/HAP-9.5 (Figure S7).

In order to assess the WGS activity of the apatite-supported catalysts quantitatively, we measured specific reaction rates in the reformate-type mixture between 573 and 673 K. Figure 4

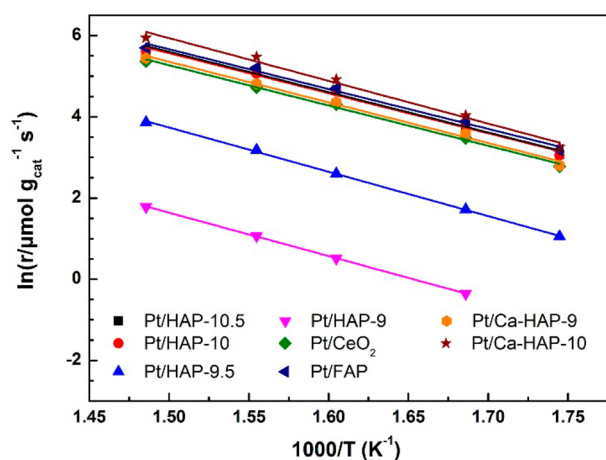


Figure 4. WGS rates in reformate-type feed gas in the temperature range 573–673 K.

shows Arrhenius plots of the determined reaction rates, from which activation energies E_{act} were derived. These are given in Table 2 together with the specific reaction rates at 573 K and corresponding turnover frequencies (TOFs) calculated from Pt dispersion (Table 1). Reaction rates varied only marginally with space velocity (Figure S8 in the Supporting Information), demonstrating that diffusion within the catalyst bed had negligible impact under our kinetic test conditions. The table also includes such data of Pt WGS catalysts from the literature^{7,13,45–49} that were tested in product-containing (CO₂, H₂) reaction mixtures. The WGS activation energies of the apatite-supported catalysts are at the upper end of the range reported for those literature catalysts but are close to the 82 kJ mol⁻¹ found for the Pt/CeO₂ catalyst prepared here. Note that

Thinin et al.⁷ reported a somewhat lower value of 65 kJ mol⁻¹ for a 2% Pt/CeO₂ catalyst that exhibited also a rather moderate specific WGS reaction rate (Table 2). This shows that precursor materials and preparation methods are very important for the activity of WGS catalysts supported on reducible oxides where metal–support interactions³² play a significant role.

Figure 4 and the tabulated reaction rates confirm that all Pt/apatite catalysts are more WGS active than our Pt/CeO₂ catalyst except for Pt/HAP-9 and Pt/HAP-9.5. In fact, the specific reaction rates are very similar for the catalysts supported on apatites with Ca/P \geq 1.75 and exceed that of the ceria-supported catalyst by ca. 50% in the case of Pt/FAP and Pt/Ca-HAP-10. This assessment also stands when TOFs are considered. It is unclear whether turnover frequencies over the apatite catalysts are indeed lower than those over our Pt/CeO₂ catalyst because of the uncertainty associated with Pt dispersion on CeO₂ (vide supra). We employed the lowest plausible dispersion for calculation so that the tabulated TOF is the upper limit for this Pt/CeO₂ catalyst. Even if correct, that value only would signal that larger Pt particles on CeO₂ are more WGS active than smaller particles on apatite supports. However, a larger Pt fraction will be inaccessible in larger particles, reducing the utilization efficiency of the precious metal. Therefore, from a practical (i.e., cost) point of view it is more interesting to consider reaction rates normalized to Pt amount, which are included in Table 2 as well. These also facilitate comparisons with literature catalysts, as they account for differing noble-metal contents. From these normalized reaction rates it is obvious that the best apatite-supported catalysts rank among the top Pt WGS catalysts reported so far. Only a strongly sodium promoted Pt/TiO₂ catalyst gave a higher specific WGS rate at 573 K.⁴⁵ The latter catalyst was tested in a rather diluted mixture with no CO₂ present, however.

Reaction Intermediates. Figure 5 shows in situ FTIR spectra of the Pt/HAP-10.5 catalysts recorded at 523 K under N₂ and a WGS mixture consisting of 1.9% CO and 3.2% H₂O in He. The spectrum under an N₂ atmosphere is practically identical with that reported by Canepa et al. for hydroxyapatite nanoparticles.⁵¹ Accordingly, the bands in the 1300–1600 cm⁻¹ range are due to carbonate species, the band centered at 1630 cm⁻¹ originates from H₂O molecules (bending mode) on the surface, and the group of bands between 1900 and 2250 cm⁻¹ are overtones and combinations of the fundamental phosphate modes below 1250 cm⁻¹ (cf. Figure 1). In addition there is a broad and asymmetric adsorption spreading out from 2250 to 3800 cm⁻¹ which arises from superposition of stretching modes of surface hydroxy groups and H₂O molecules involved in H bonding.⁵¹ Several additional bands emerged after switching to the WGS atmosphere. The intense band at 2051 cm⁻¹ can be readily assigned to CO bonded to Pt on the basis of literature (2059 cm⁻¹).⁵² On the other hand, bands at 1349, 1378, 1588, and 2858 cm⁻¹ agree very well with the symmetric ($\nu_s(\text{CO})$) and asymmetric C–O stretching ($\nu_{\text{as}}(\text{CO})$) and the C–H bending ($\delta(\text{CH})$) and stretching ($\nu(\text{CH})$) modes reported for formate anions in aqueous solution ($\nu_s(\text{CO})$ 1351 cm⁻¹, $\delta(\text{CH})$ 1383 cm⁻¹, $\nu_{\text{as}}(\text{CO})$ 1585 cm⁻¹, $\nu(\text{CH})$ 2803)⁵³ and icy matter ($\nu_s(\text{CO})$ 1350 cm⁻¹, $\delta(\text{CH})$ 1380 cm⁻¹, $\nu_{\text{as}}(\text{CO})$ 1580 cm⁻¹).⁵⁴ Furthermore, the band at 1756 cm⁻¹ matches well with the stretching mode reported for gaseous formic acid at $\nu(\text{CO})$ 1767 cm⁻¹.⁵⁵ Thus, formate appears to be the key

Table 2. Specific WGS Reaction Rates r of Pt-Based Catalysts at 573 K and Atmospheric Pressure

catalyst	Pt (wt %)	r ($\mu\text{mol}_{\text{CO}} \text{g}_{\text{cat}}^{-1} \text{s}^{-1}$)	r ($\text{mol}_{\text{CO}} \text{mol}_{\text{Pt}}^{-1} \text{s}^{-1}$)	TOF (s^{-1})	E_{act} (kJ mol^{-1})	ref
Pt/HAP-10.5	0.77	21.6	0.548	0.55	83	this work
Pt/HAP-10	0.74	21.2	0.558	0.58	82	this work
Pt/HAP-9.5	0.78	2.9	0.072	0.10	90	this work
Pt/HAP-9	0.82	1.7 ^a	0.040 ^a	0.05	89	this work
Pt/FAP	0.78	24.0	0.596	0.60	81	this work
Pt/Ca-HAP-10	0.79	24.9	0.617		87	this work
Pt/Ca-HAP-9	0.73	16.5	0.444		83	this work
Pt/CeO ₂	0.74	16.0	0.424	0.73 ^b	82	this work
Pt/CeO ₂	2	15 ^c	0.146		65	7
Pt/CeO ₂ /Al ₂ O ₃	0.9	27 ^c	0.585		70	7
Pt/ZrO ₂	1.5	20 ^c	0.260		58	7
Pt/TiO ₂	1.9	39 ^c	0.400		23	7
Pt/Fe ₂ O ₃	1.5	6 ^c	0.078		44	7
Pt-4Na-TiO ₂	1	58.6 ^d	1.143	3.82	80	45
Pt/MgO-CeO ₂	1	2.8 ^d	0.055			46
Pt/6VCeO ₂	1.15	3.8 ^e	0.064		86	47
Pt/ZrO ₂	0.95	2.33 ^f	0.048	0.41		48
Pt/Ti/ZrO ₂	0.97	7.51 ^f	0.151	0.43		48
Pt/CeO ₂	0.5	6.3 ^g	0.248	0.33		13
Pt/Ca _{0.5} Ce _{0.5} O _{1.5}	0.5	12.5 ^g	0.490	0.65		13
Pt/Ce(La) _x O _x NaCN leached	3.06 ^h	73.7 ⁱ	0.470		75	49
Pt/Ce(La) _x O _x	4.15 ^h	45 ⁱ	0.211		75	49

^aRate at 623 K. ^bCalculated for 58% Pt dispersion. ^cReactant composition: 10% CO, 20% H₂O, 10% CO₂, 30% H₂, 30% Ar. ^dReactant composition: 2.83% CO, 5.66% H₂O, 37.74% H₂, 53.77% He. ^eReactant composition: 6.0% CO, 60.0% H₂O, 1.6% CO₂, 16.0% H₂, 0.4% CH₄, 16.0% N₂. ^fReactant composition: 7.0% CO, 22.0% H₂O, 8.5% CO₂, 37% H₂, 25.5% N₂. ^gReactant composition: 3.0% CO, 26.2% H₂, 29.9% H₂, 3.7% N₂, 37.2% He. Pt dispersion was estimated at 75% assuming 1.5 nm hemispherical particles according to an established method.^{29,30} ^hPt content calculated from bulk atomic Pt/Ce/La ratio assuming CeO₂ and La₂O₃. ⁱReactant composition: 11% CO, 26% H₂O, 7% CO₂, 26% H₂, 26% He.

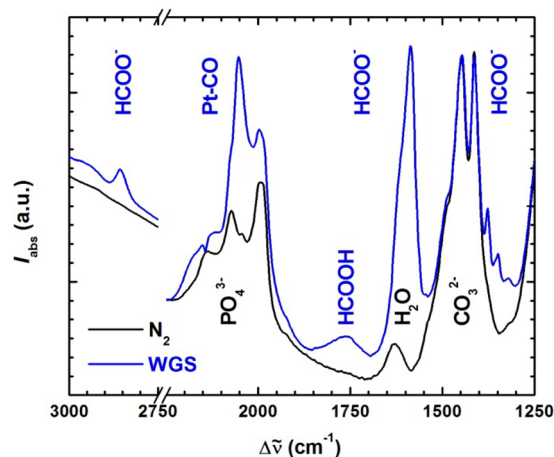


Figure 5. In situ FTIR spectra of Pt/HAP-10.5 catalyst under an N₂ and WGS atmosphere at 523 K.

intermediate in the WGS reaction over apatite-supported Pt catalysts.

Catalyst Stability. Stability of the Pt/HAP-10.5 and Pt/CeO₂ catalysts was tested in the reformate-type mixture at 673 K (Figure 6). CO conversion dropped somewhat over both catalysts during the first 24 h but then remained constant at ~52% for Pt/HAP-10.5 and ~47% for Pt/CeO₂ for the remainder of the 100 h experiment. This demonstrates that the apatite-supported catalyst retained its superior WGS performance during continuous operation. It was characterized by XRD, BET, TEM, and TPO measurements after this test. The XRD pattern of the stability-tested sample was identical with that of the fresh sample (Figure S9 in the Supporting

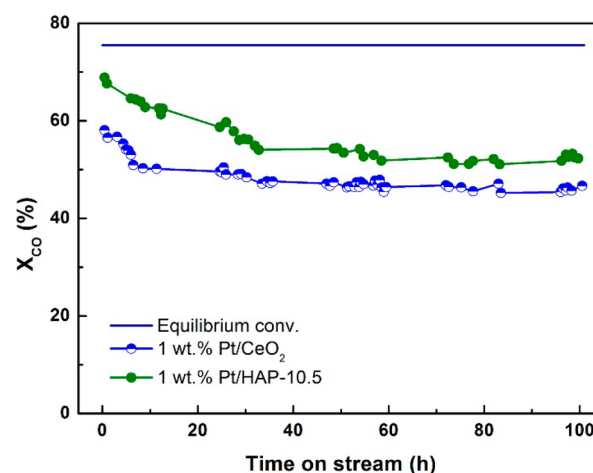


Figure 6. Stability of Pt/HAP-10.5 and Pt/CeO₂ catalysts in reformate-type feed gas at 673 K.

Information), while S_{BET} had decreased from 78 m² g⁻¹ to 53 m² g⁻¹ with a concomitant increase of the average pore size from 10 to 16 nm (Figure S10 in the Supporting Information). This may indicate blocking of the smaller support pores. TPO experiments yielded a weak CO₂ signal (m/z 44) between 523 and 823 K, but this was again practically identical with that from a fresh catalyst sample (Figure S11 in the Supporting Information). In addition, the H₂O signals (m/z 18) were rather similar before and after WGS testing (Figure S11). Thus, CO₂ evolution was likely due to contraction of airborne carbonaceous contaminants during handling of the samples under ambient atmosphere, and coke formation remained below the detection level of our facilities after 100 h operation

of Pt/HAP-10.5 in reformat. Finally, Figure 7 shows TEM images and Pt particle size distributions of the fresh and used

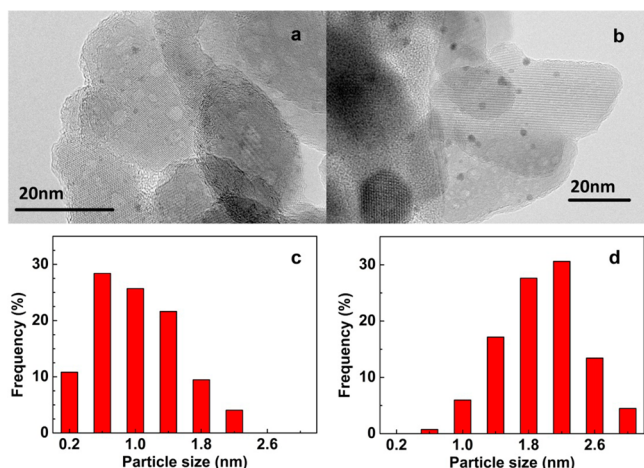


Figure 7. TEM images and Pt particle size distributions of fresh (a, c) and used (b, d) Pt/HAP-10.5 catalyst samples.

Pt/HAP-10.5 samples. The Pt particle size had increased slightly from ca. 1 nm to ca. 2 nm after 100 h, but it remained quite uniform. This minor Pt particle growth and decrease of surface area might be responsible for the initial X_{CO} decline during the stability test, but the rapid stabilization of CO conversion shows that these apatite catalysts are structurally stable under typical WGS conditions at 673 K.

DISCUSSION

The high-temperature WGS activity of Pt/apatite catalysts clearly correlates with the Ca/P ratio of the support material. Addition of Ca is known to promote the WGS conversion rates on Pt/CeO₂^{13,56} and Pt/TiO₂⁵⁷ significantly. Incorporation of Ca²⁺ into ceria and titania lattices enhances the reducibility and mobility of oxygen.^{13,57} Liganiso et al. suggested that this improves the mobility of O-bound reaction intermediates such as formates, carbonates, and carboxylates and thus facilitates their decomposition into CO₂ and H₂.¹³ Kondarides and co-workers attributed the higher reaction rates to the creation of oxygen vacancies at the Pt support interface that are capable of adsorption and activation of both CO and H₂O.^{56,57} Neither of these scenarios can apply in the present case, since apatites are not easily reduced and TPR peaks below 773 K can be readily attributed to PtO_x species in our catalysts.

The noble metal is generally thought to be responsible for CO activation in supported WGS catalysts, while the oxide activates H₂O.² The intense Pt–CO band in the in situ FTIR spectrum suggests that CO is activated on Pt in HAP catalysts as well. It is also plausible that apatites assume the H₂O activating role in the catalysts investigated here, given their very large hydrophilicity.⁵⁸ Ab initio calculations for the two most important HAP surfaces confirmed that their affinity is high for H₂O.^{59,60} While H₂O adsorbs molecularly on the (001) surface, it dissociates spontaneously on the (010) surface in a barrierless, highly exothermic process (–250 to –320 kJ mol^{–1}), giving rise to new surface terminations (Ca–OH and PO–H).^{51,60} Calculated H₂O binding energies (–50 to –100 kJ mol^{–1}) agree well with calorimetric adsorption enthalpies, revealing also that the affinity of the reconstructed (010)

surface for H₂O remains nearly as high as that of the (010) surface.⁶⁰

Combining IR spectroscopy and microgravimetry, it has been inferred that H₂O molecules are coordinated approximately in a 1:1 ratio to surface Ca²⁺ ions in the first hydration layer.⁵⁸ The computational modeling provided more detailed insight into the interaction between H₂O and HAP at the molecular level in addition. Unsaturated surface Ca²⁺ cations act as Lewis acids to which water molecules coordinate through their O atom, while a rather strong H bond is simultaneously formed with a basic O atom of a neighboring PO₄^{3–} group.^{60,61} Hence, the large H₂O binding energies on HAP surfaces are due to a synergetic bonding situation that renders the adsorbed H₂O molecules highly polarized if not dissociated. In these states H₂O will be very reactive toward electrophilic molecules such as CO. The dual H₂O bonding also allows for a rationale for the observed WGS activity dependence on Ca/P ratio: Ca²⁺ ions are essential for anchoring H₂O, and thus their concentration determines the density of these reactant molecules on the HAP surface in the first place. The secondary H bonding requires a sufficient number of accessible O atoms from PO₄^{3–} units in the vicinity of the cations, on the other hand. This sets an upper limit for the number of fully activated H₂O molecules on the HAP surface, which could explain why WGS activity levels off around Ca/P ≈ 1.75. Note that the surface Ca/P ratio (Table 1) approached the value of stoichiometric HAP (i.e., 1.67) at this overall composition. Presumably, H₂O activation benefits from an optimum balance between Ca²⁺ and PO₄^{3–} ions on the apatite surface. Activation of additional H₂O molecules is probably not feasible via simultaneous coordination to Ca²⁺ and H bonding to PO₄^{3–} ions above that boundary. Obviously this implies that H₂O activation is a key step in the WGS reaction on these Pt/apatite catalysts. Preliminary kinetic analyses reveal that the H₂O reaction order n is noticeably larger for Pt/HAP-10.5 ($n = 0.81$) than for Pt/CeO₂ ($n = 0.55$) at 623 K, indicating a greater influence of H₂O on the apatite-supported WGS catalysts as well.

The similarity of activation energies further suggests that the rate-determining steps involve similar activated species on Pt WGS catalysts supported on apatite and reducible oxides such as CeO₂. The exact nature of the relevant intermediates and the mechanistic route(s) for the WGS reaction are still a matter of debate.² Two general types of reaction pathways are under discussion in the case of Pt/CeO₂: i.e., associative mechanisms involving e.g. formate^{62,63} and/or carboxylate species⁶⁴ and regenerative redox routes involving oxygen transfer from the support.⁶⁵ Such a redox mechanism does not appear to be viable for WGS on Pt/apatites, considering the irreducible character of the support. Formate species have been frequently proposed^{62,63} as crucial intermediates in associative mechanisms, on the other hand, and their decomposition into CO₂ is deemed to be rate-determining.² The in situ FTIR analysis of the Pt/HAP-10.5 catalyst under the CO/H₂O/He atmosphere (Figure 5) strongly suggests that formate is also the key reaction intermediate in the WGS reaction over apatite-supported catalysts.

Ab initio calculations have also been employed to investigate the interaction of formic acid with HAP surfaces.⁵¹ Formic acid was found to adsorb molecularly on the (001) surface with binding energies of around 190 kJ mol^{–1} but to dissociate spontaneously on the water-reconstructed (010) surface with a formate ion binding energy of ca. 250 kJ mol^{–1}.⁵¹ Formate ions can also form on the (001) surface, albeit with a somewhat

lower binding energy (ca. 170 kJ mol⁻¹).⁵¹ This demonstrates that apatite surfaces can stabilize formate ions rather well once they are formed there. Formate acts as a bidentate ligand with its two O atoms coordinating to two separate Ca²⁺ ions on the (001) HAP surface.⁵¹ The bonding situation is more complex on the reconstructed (010) surface, where one formate O atom bonds to two Ca²⁺ ions. The other formate O atom bonds to a third Ca²⁺ ion and also forms a hydrogen bond with the nearby H atom of hydroxide ions resulting from H₂O dissociation on the (010) surface.⁵¹ Similar adducts between Pt-activated CO and apatite-activated H₂O molecules can be readily envisioned as intermediates of the WGS reaction on apatite-supported catalysts. The requirement of multiple Ca²⁺ surface ions for formation of formate-like activated complexes may also play a role in the large sensitivity of WGS reaction rates toward the surface Ca/P ratio of apatites. Moreover, formate reaction intermediates may explain why apatite-supported catalysts were less WGS active than the Pt/CeO₂ catalyst below 523 K (Figure 3). Decomposition of intermediary formate adducts could be hampered on Pt/HAP at lower temperatures because of their better stabilization on apatite than on CeO₂ surfaces. Thus, the observed WGS activity trends of Pt/apatite catalysts can be well understood in the framework of an associative mechanism involving formate-like reaction intermediates.

Irrespective of mechanistic details, it is obvious that the outstanding high-temperature WGS activity of optimized Pt/apatite catalysts is due to the very efficient H₂O activation on the ionic apatite surface. In fact, H₂O is more difficult to activate than CO between the two WGS reactants, due to its thermodynamic stability.² The present results suggest that H₂O activation is superior on apatites in comparison with CeO₂, where the WGS reaction is aided by facile redox cycling of the latter material. The specific HTS reaction rate on the Pt/CeO₂ catalyst tested here is among the highest for such Pt catalysts supported on reducible oxides reported in the literature (Table 2). Therefore, the oxygen storage capacity of reducible oxides appears to be less important for improving the (high-temperature) WGS activity than efficient H₂O activation. Evidently the latter can be more readily achieved on suitable ionic materials such as apatites. However, note that structural OH⁻ ions of HAP are not involved in H₂O adsorption and activation as H₂O moves away from those basic ions.⁶⁰ Therefore, it is not surprising that their substitution with F⁻ ions has no effect on the WGS activity and reaction rates on optimized Pt/FAP and Pt/HAP are practically the same.

CONCLUSION

The water-gas shift activity of Pt/apatite catalysts is strongly correlated with increasing Ca/P ratio in the support material, until it levels off around Ca/P ≈ 1.75. The WGS activity of such optimized catalysts exceeds that of a highly active Pt/CeO₂ catalyst prepared here with the same noble metal loading above 523 K, with specific reaction rates being up to 50% higher at 573 K. This extraordinary WGS performance is attributed to superior activation of H₂O and stabilization of ensuing formate-like reaction intermediates on these hydrophilic, ionic oxides. Literature ab initio modeling studies^{59,60} indicate that simultaneous coordination of H₂O to Lewis acidic Ca²⁺ ions and H bonding to basic O atoms of PO₄³⁻ units render H₂O molecules highly polarized and thus reactive on apatite surfaces. Moreover, the apatite-supported catalysts do not exhibit any methanation activity up to 723 K but good stability, as CO conversion remained constant during a 100 h

test at 673 K after a minor initial activity loss. The latter is likely due to growth of mean Pt particle size from ca. 1 nm to ca. 2 nm, since TPO of a fresh and the stability tested sample yielded minor and practically identical CO₂ emission patterns. This very favorable set of characteristics makes Pt/apatite catalysts promising candidates for application in single-stage, high-temperature WGS devices that require catalyst beds with large spatial and minimal mass transfer limitations such as micro and membrane reactors.

ASSOCIATED CONTENT

Supporting Information

The Supporting Information is available free of charge on the ACS Publications website at DOI: 10.1021/acscatal.5b01909.

Additional catalyst characterization data (PDF)

AUTHOR INFORMATION

Corresponding Author

*A.G.: e-mail, goldbach@dicp.ac.cn; tel, + 86 411 8437 9229.

Notes

The authors declare no competing financial interest.

ACKNOWLEDGMENTS

Financial support by the Chinese Academy of Sciences through the External Cooperation Program (Helmholtz-CAS Joint Research Group on Integrated Catalytic Technologies for Efficient Hydrogen Production, grant no. GJHZ1304) is gratefully acknowledged.

REFERENCES

- (1) Sun, Y.; Hla, S. S.; Duffy, G. J.; Cousins, A. J.; French, D.; Morpeth, L. D.; Edwards, J. H.; Roberts, D. G. *Appl. Catal., A* **2010**, *390*, 201–209.
- (2) Azzam, K. G.; Babich, I. V.; Seshan, K.; Lefferts, L. *J. Catal.* **2007**, *251*, 153–162.
- (3) Kalamaras, C. M.; Dionysiou, D. D.; Efstathiou, A. M. *ACS Catal.* **2012**, *2*, 2729–2742.
- (4) Jacobs, G.; Chenu, E.; Patterson, P. M.; Williams, L.; Sparks, D.; Thomas, G.; Davis, B. H. *Appl. Catal., A* **2004**, *258*, 203–214.
- (5) Panagiotopoulou, P.; Kondarides, D. I. *J. Catal.* **2004**, *225*, 327–336.
- (6) Liu, X. S.; Ruettinger, W.; Xu, X. M.; Farrauto, R. *Appl. Catal., B* **2005**, *56*, 69–75.
- (7) Thinon, O.; Diehl, F.; Avenier, P.; Schuurman, Y. *Catal. Today* **2008**, *137*, 29–35.
- (8) Piermartini, P.; Schuhmann, T.; Pfeifer, P.; Schaub, G. *Top. Catal.* **2011**, *54*, 967–976.
- (9) Bi, Y.; Xu, H.; Li, W.; Goldbach, A. *Int. J. Hydrogen Energy* **2009**, *34*, 2965–2971.
- (10) Ma, D. H.; Lund, C. R. F. *Ind. Eng. Chem. Res.* **2003**, *42*, 711–717.
- (11) Li, H.; Goldbach, A.; Li, W.; Xu, H. *J. Membr. Sci.* **2007**, *299*, 130–137.
- (12) Zalc, J. M.; Sokolovskii, V.; Löffler, D. G. *J. Catal.* **2002**, *206*, 169–171.
- (13) Liganiso, L. Z.; Jacobs, G.; Azzam, K. G.; Graham, U. M.; Davis, B. H.; Cronauer, D. C.; Kropf, A. J.; Marshall, C. L. *Appl. Catal., A* **2011**, *394*, 105–116.
- (14) Venugopal, A.; Scurrrell, M. S. *Appl. Catal., A* **2003**, *245*, 137–147.
- (15) Zhao, K.; Qiao, B.; Wang, J.; Zhang, Y.; Zhang, T. *Chem. Commun.* **2011**, *47*, 1779–1781.
- (16) Gbantani, V. C.; Lomate, S. T.; Dongare, M. K.; Umbarkar, S. B. *Green Chem.* **2013**, *15*, 1211–1217.

- (17) Ogo, S.; Onda, A.; Iwasa, Y.; Hara, K.; Fukuoka, A.; Yanagisawa, K. *J. Catal.* **2012**, *296*, 24–30.
- (18) Tsuchida, T.; Kubo, J.; Yoshioka, T.; Sakuma, S.; Takeguchi, T.; Ueda, W. *J. Catal.* **2008**, *259*, 183–189.
- (19) Yan, B.; Tao, L. Z.; Liang, Y.; Xu, B. Q. *ACS Catal.* **2014**, *4*, 1931–1943.
- (20) Domínguez, M. I.; Romero-Sarria, F.; Centeno, M. A.; Odriozola, J. A. *Appl. Catal., B* **2009**, *87*, 245–251.
- (21) Phonthammachai, N.; Ziyi, Z.; Jun, G.; Fan, H. Y.; White, T. J. *Gold Bull.* **2008**, *41*, 42–50.
- (22) Carvalho, D. C.; Pinheiro, L. G.; Campos, A.; Millet, E. R. C.; de Sousa, F. F.; Filho, J. M.; Saraiva, G. D.; da Silva Filho, E. C.; Fonseca, M. G.; Oliveira, A. C. *Appl. Catal., A* **2014**, *471*, 39–49.
- (23) Huang, J.; Wang, L.-C.; Liu, Y.-M.; Cao, Y.; He, H.-Y.; Fan, K.-N. *Appl. Catal., B* **2011**, *101*, 560–569.
- (24) Takarrumt, N.; Kacimi, M.; Bozon-Verduraz, F.; Liotta, L. F.; Ziyad, M. *J. Mol. Catal. A: Chem.* **2013**, *377*, 42–50.
- (25) Gangarajula, Y.; Kedharnath, R.; Gopal, B. *Appl. Catal., A* **2015**, *506*, 100–108.
- (26) Sugiyama, S.; Miyamoto, T.; Hayashi, H.; Moffat, J. B. *J. Mol. Catal. A: Chem.* **1998**, *135*, 199–208.
- (27) Kozlowski, J. T.; Davis, R. J. *ACS Catal.* **2013**, *3*, 1588–1600.
- (28) Luengnaruemitchai, A.; Osuwan, S.; Gulari, E. *Catal. Commun.* **2003**, *4*, 215–221.
- (29) Cavusoglu, G.; Miao, D.; Lichtenberg, H.; Carvalho, H. W. P.; Xu, H.; Goldbach, A.; Grunwaldt, J.-D. *Appl. Catal., A* **2015**, *504*, 381–390.
- (30) Perrichon, V.; Retailleau, L.; Bazin, P.; Daturi, M.; Lavalley, J. C. *Appl. Catal., A* **2004**, *260*, 1–8.
- (31) Jacobs, G.; Ricote, S.; Graham, U. M.; Patterson, P. M.; Davis, B. H. *Catal. Today* **2005**, *106*, 259–264.
- (32) Bernal, S.; Calvino, J. J.; Cauqui, M. A.; Gatica, J. M.; López Cartes, C.; Pérez Omil, J. A.; Pintado, J. M. *Catal. Today* **2003**, *77*, 385–406.
- (33) Liu, B.; Goldbach, A.; Xu, H. *Catal. Today* **2011**, *171*, 304–311.
- (34) Zhang, Y.; Wang, J.; Yin, J.; Zhao, K.; Jin, C.; Huang, Y.; Jiang, Z.; Zhang, T. *J. Phys. Chem. C* **2010**, *114*, 16443–16450.
- (35) Chen, W.; Huang, Z.; Liu, Y.; He, Q. *Catal. Commun.* **2008**, *9*, 516–521.
- (36) Lynn, A. K.; Bonfield, W. *Acc. Chem. Res.* **2005**, *38*, 202–207.
- (37) Lafon, J. P.; Champion, E.; Bernache-Assollant, D. *J. Eur. Ceram. Soc.* **2008**, *28*, 139–147.
- (38) Yasukawa, A.; Kandori, K.; Ishikawa, T. *Calcif. Tissue Int.* **2003**, *72*, 243–250.
- (39) Boukha, Z.; Kacimi, M.; Pereira, M. F. R.; Faria, J. L.; Figueiredo, J. L.; Ziyad, M. *Appl. Catal., A* **2007**, *317*, 299–309.
- (40) Boukha, Z.; Kacimi, M.; Ziyad, M.; Ensuque, A.; Bozon-Verduraz, F. *J. Mol. Catal. A: Chem.* **2007**, *270*, 205–213.
- (41) Yu, C.; Ge, Q.; Xu, H.; Li, W. *Catal. Lett.* **2006**, *112*, 197–201.
- (42) Zhang, Y.; Zhou, Y.; Qiu, A.; Wang, Y.; Xu, Y.; Wu, P. *Catal. Commun.* **2006**, *7*, 860–866.
- (43) Zhang, Y.; Zhou, Y.; Huang, L.; Zhou, S.; Sheng, X.; Wang, Q.; Zhang, C. *Chem. Eng. J.* **2015**, *270*, 352–361.
- (44) Borgna, A.; Le Normand, F.; Garetto, T.; Apesteguia, C. R.; Moraweck, B. *Catal. Lett.* **1992**, *13*, 175–188.
- (45) Zhu, X.; Shen, M.; Lobban, L. L.; Mallinson, R. G. *J. Catal.* **2011**, *278*, 123–132.
- (46) Duarte de Farias, A. M.; Barandas, A. P. M. G.; Perez, R. F.; Fraga, M. A. *J. Power Sources* **2007**, *165*, 854–860.
- (47) Duarte de Farias, A. M.; Bargiela, P.; Rocha, M. d. G. C.; Fraga, M. A. *J. Catal.* **2008**, *260*, 93–102.
- (48) Hwang, K.-R.; Ihm, S.-K.; Park, S.-C.; Park, J.-S. *Int. J. Hydrogen Energy* **2013**, *38*, 6044–6051.
- (49) Fu, Q.; Saltsburg, H.; Flytzani-Stephanopoulos, M. *Science* **2003**, *301*, 935–938.
- (50) Bergeret, G.; Gallezot, P. In *Handbook of Heterogeneous Catalysis*; Ertl, G., Knözinger, H., Schüth, F., Weitkamp, J., Eds.; Wiley-VCH: Weinheim, Germany, 2008; Vol. 3, pp 738–765.
- (51) Canepa, P.; Chiatti, F.; Corno, M.; Sakhno, Y.; Martra, G.; Ugliengo, P. *Phys. Chem. Chem. Phys.* **2011**, *13*, 1099–1111.
- (52) Kuriyama, M.; Tanaka, H.; Ito, S.; Kubota, T.; Miyao, T.; Naito, S.; Tomishige, K.; Kunimori, K. *J. Catal.* **2007**, *252*, 39–48.
- (53) Ito, K.; Bernstein, H. J. *Can. J. Chem.* **1956**, *34*, 170–178.
- (54) Schutte, W. A.; Boogert, A. C. A.; Tielens, A. G. G. M.; Whittet, D. C. B.; Gerakines, P. A.; Chiar, J. E.; Ehrenfreund, P.; Greenberg, J. M.; van Dishoeck, E. F.; de Graauw, T. *Astron. Astrophys.* **1999**, *343*, 966–976.
- (55) Maçôas, E. M. S.; Lundell, J.; Pettersson, M.; Khriachtchev, L.; Fausto, R.; Räsänen, M. *J. Mol. Spectrosc.* **2003**, *219*, 70–80.
- (56) Panagiotopoulou, P.; Papavasiliou, J.; Avgouropoulos, G.; Ioannides, T.; Kondarides, D. I. *Chem. Eng. J.* **2007**, *134*, 16–22.
- (57) Panagiotopoulou, P.; Kondarides, D. I. *Appl. Catal., B* **2011**, *101*, 738–746.
- (58) Bertinetti, L.; Tampieri, A.; Landi, E.; Ducati, C.; Midgley, P. A.; Coluccia, S.; Martra, G. *J. Phys. Chem. C* **2007**, *111*, 4027–4035.
- (59) Astala, R.; Stott, M. J. *Phys. Rev. B: Condens. Matter Mater. Phys.* **2008**, *78*, 075427.
- (60) Corno, M.; Busco, C.; Bolis, V.; Tosoni, S.; Ugliengo, P. *Langmuir* **2009**, *25*, 2188–2198.
- (61) Bolis, V.; Busco, C.; Martra, G.; Bertinetti, L.; Sakhno, Y.; Ugliengo, P.; Chiatti, F.; Corno, M.; Roveri, N. *Philos. Trans. R. Soc., A* **2012**, *370*, 1313–1336.
- (62) Shido, T.; Iwasawa, Y. *J. Catal.* **1993**, *141*, 71–81.
- (63) Jacobs, G.; Davis, B. H. *Int. J. Hydrogen Energy* **2010**, *35*, 3522–3536.
- (64) Grabow, L. C.; Gokhale, A. A.; Evans, S. T.; Dumesic, J. A.; Mavrikakis, M. *J. Phys. Chem. C* **2008**, *112*, 4608–4617.
- (65) Gorte, R. J.; Zhao, S. *Catal. Today* **2005**, *104*, 18–24.